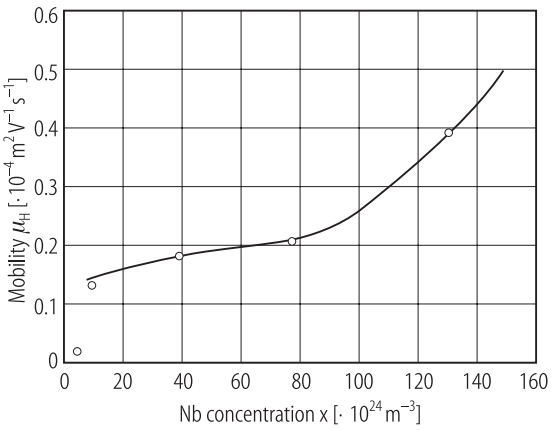

Fig. 1A-10-180. $BaTiO_3$ (Nb doped, n-type). μ_H vs. x for $BaNb_x^{V}Ti_x^{III}Ti_{1-2x}^{IV}O_3$ [77Fel]. μ_H: Hall mobility of charge carriers. x: Nb concentration.

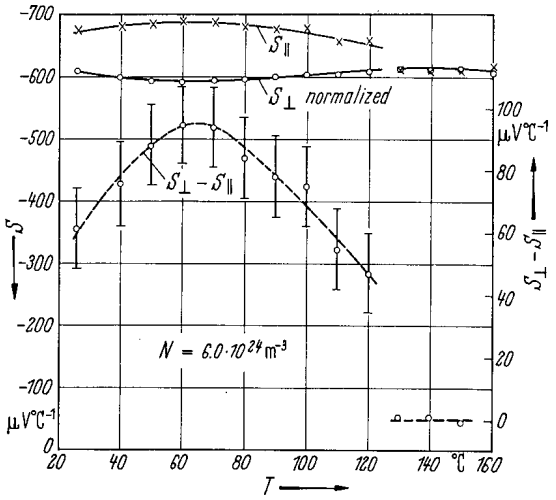

Fig. 1A-10-181. $BaTiO_3$ (reduced, n-type). *S* vs. *T* [67Ber]. *S:* Seebeck coefficient. *N:* carrier concentration estimated from the Hall coefficient.

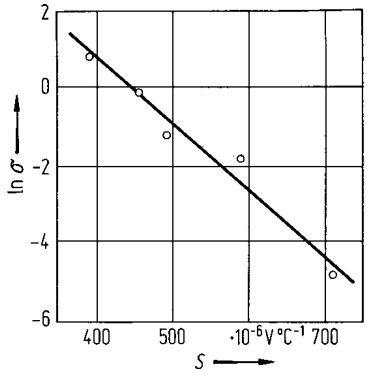

Fig. 1A-10-182. $BaTiO_3$ (semiconducting). ln σ vs. S for different semiconducting crystals containing small amount of rare earth (La, Gd, Dy) [71Bur]. σ in $\Omega^{-1}cm^{-1}$. *S:* Seebeck coefficient. T = 140 °C.

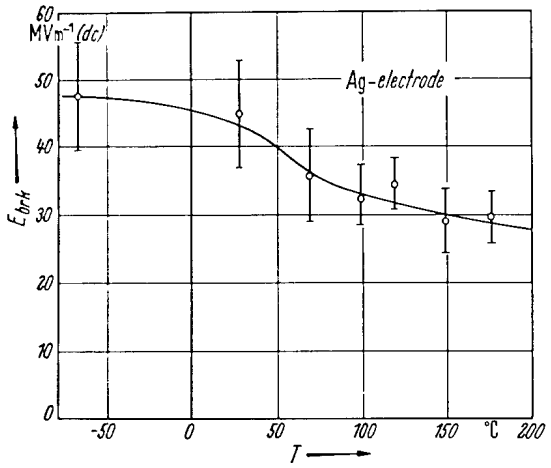

Fig. 1A-10-183. $BaTiO_3$ (0.05% Fe_2O_3 doped). E_{brk} vs. T along the c-axis [58Inu]. E_{brk}: breakdown field strength.

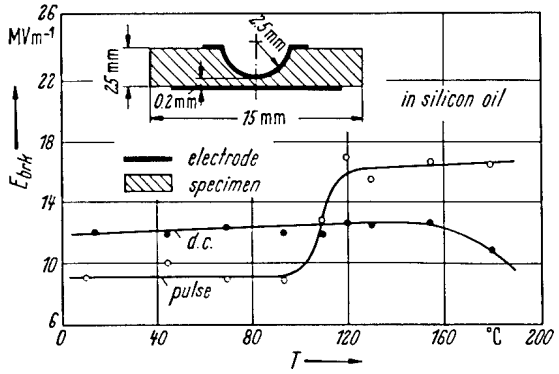

Fig. 1A-10-184. $BaTiO_3$ (ceramics). E_{brk} vs. T [64Ued].
E_{brk}: breakdown field strength.

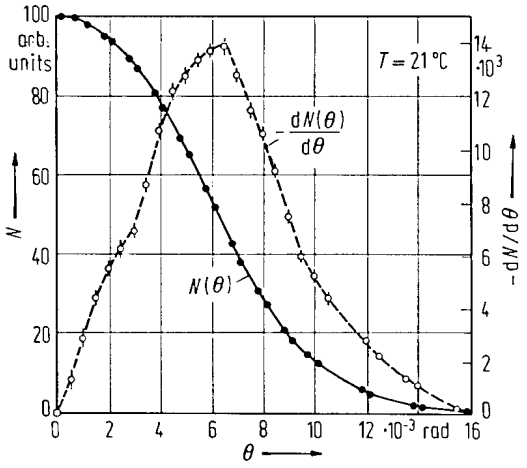

Fig. 1A-10-185. $BaTiO_3$. $N(\theta)$, $dN(\theta)/d\theta$ vs. θ [73Sue]. $N(\theta)$: counting rate of angular correlation under applied electric field.

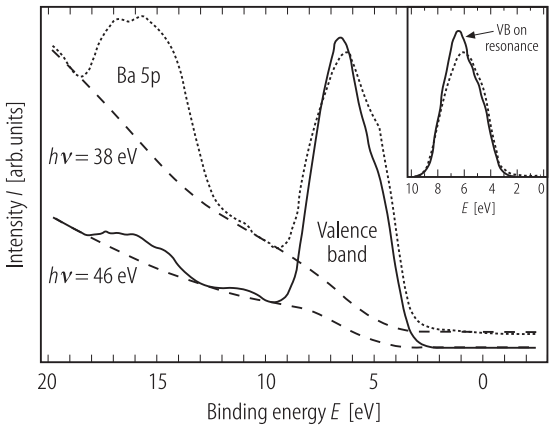

Fig. 1A-10-186. $BaTiO_3$. Ultraviolet photoemission spectra of vacuum-fractured (100) surface [93Hud]. *I:* photoelectron intensity. *E:* binding energy referenced from the bottom of the conduction band. Parameter: $h\nu$, incident photon energy. Insert shows results of substraction of an inelastic background.

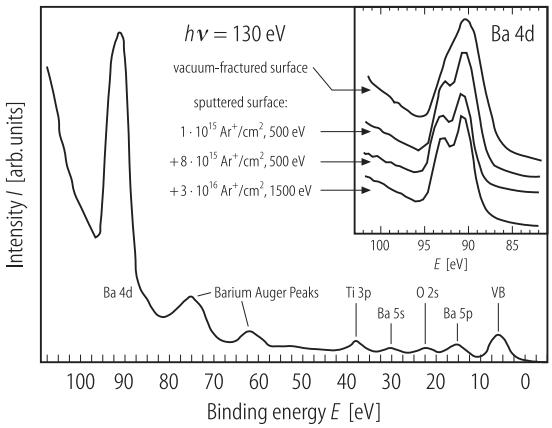

Fig. 1A-10-187. $BaTiO_3$. Ultraviolet photoemission spectra of vacuum-fractured (100) surface [93Hud]. *I:* photoelectron intensity. *E:* binding energy referenced from the bottom of the conduction band. The insert shows the evolution of the Ba 4d emissions from a surface which has been irradiated with Ar^+ ions with the incremental dose and energy.

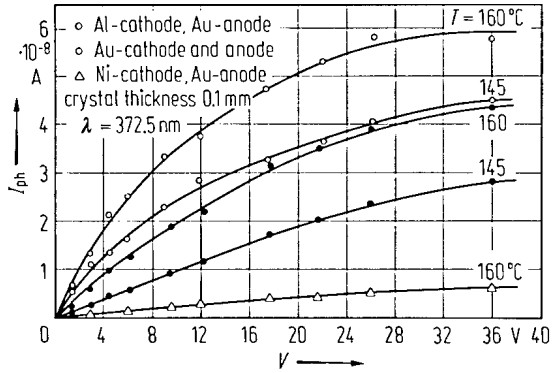

Fig. 1A-10-188. $BaTiO_3$. I_{ph} vs. V [63Cox]. Parameter: various cathode materials. I_{ph}: photocurrent, V: applied potential.

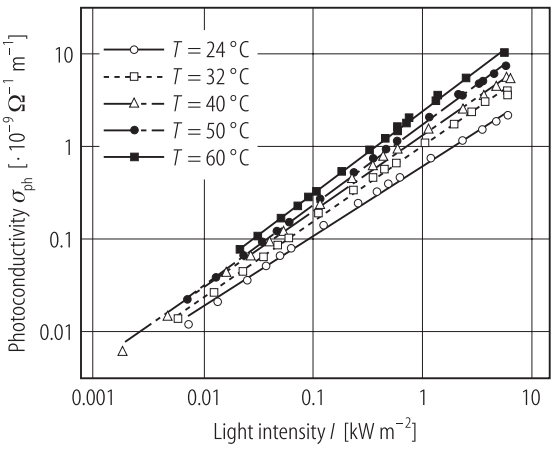

Fig. 1A-10-189. $BaTiO_3$. σ_{ph} vs. I [90Hol]. σ_{ph}: photoconductivity. *I:* light intensity. λ = 488 nm of an argon-ion laser. Parameter: *T*. Exponents x of $\sigma_{ph} \sim I^x$ are 0.76...0.90.

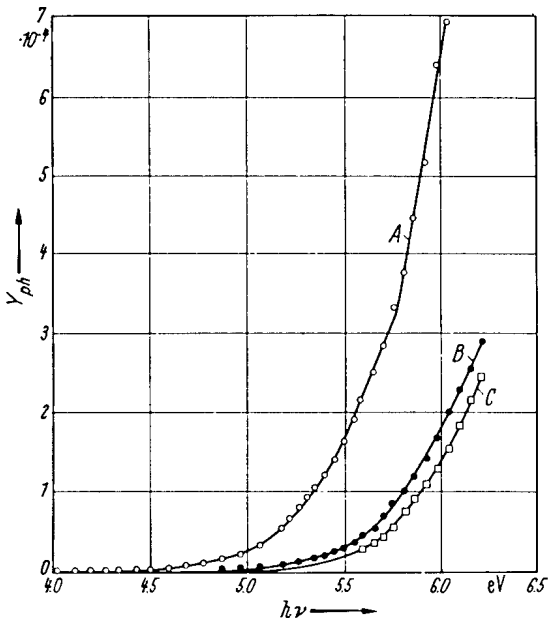

Fig. 1A-10-190. $BaTiO_3$. Y_{ph} vs. $h\nu$ [66Hud]. Y_{ph}: photoelectric yield (electrons/photon). *A*: baked at 400 °C in a vacuum of 10^{-7} Pa. *B*: exposed to dry air at atmospheric pressure for 15 min. *C*: exposed to the atmosphere for 2.5 h.

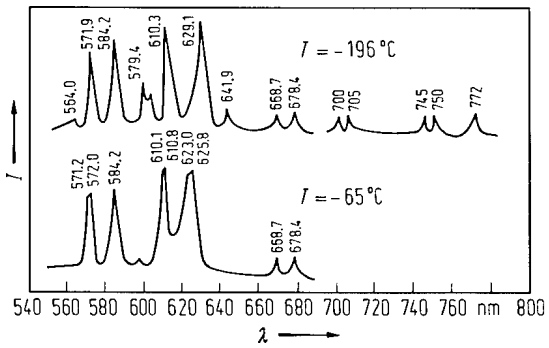

Fig. 1A-10-191. $BaTiO_3$: Sm^{3+}. I vs. λ [62Mak].
I: luminescent emission intensity. See also [65Mak].

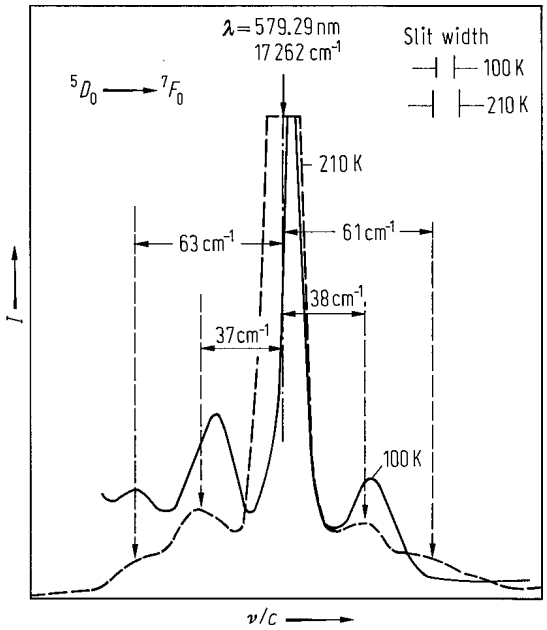

Fig. 1A-10-192. $BaTiO_3$: Eu^{3+}. *I* vs. *ν/c* [67Yam].
I: luminescent emission intensity.

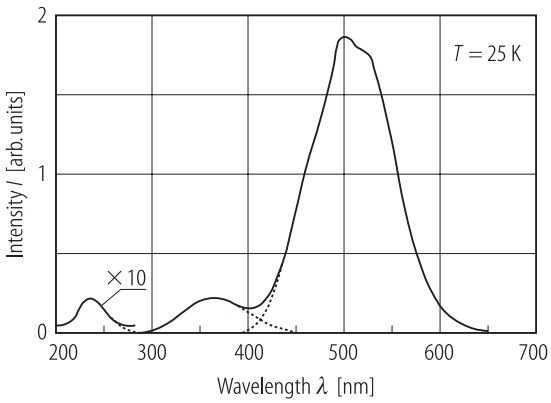

Fig. 1A-10-193. $BaTiO_3$. I vs. λ [80Agu]. *I:* luminescent emission intensity under X-ray. See also [80Gon].

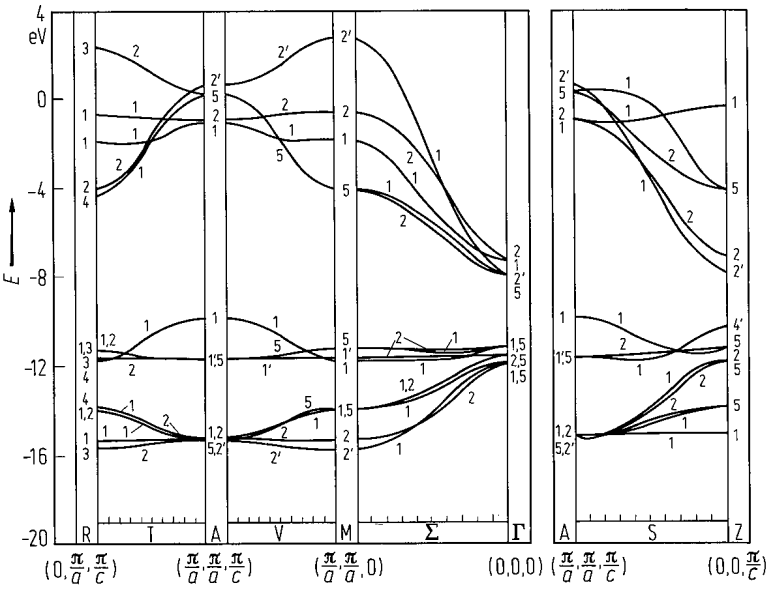

Fig. 1A-10-194. $BaTiO_3$. Energy band for the phase II [73Mic].

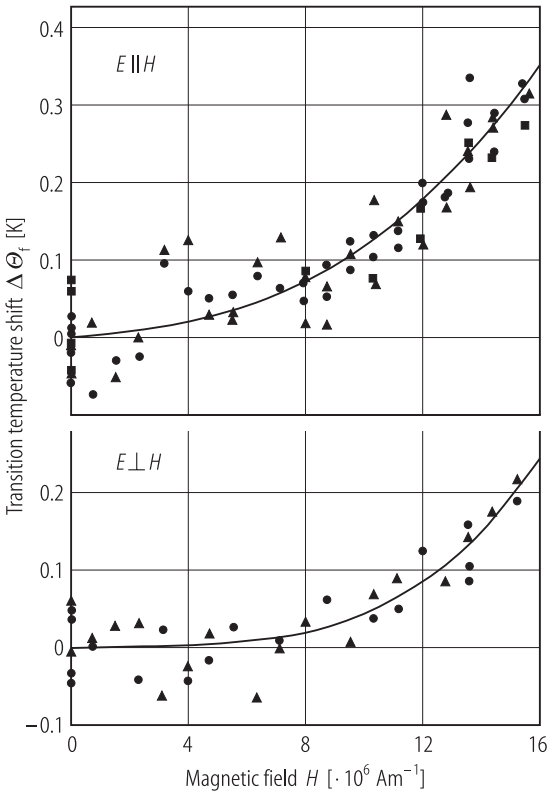

Fig. 1A-10-195. $BaTiO_3$. $\Delta\Theta_f$ vs. H [81Wag]. $\Delta\Theta_f$: shift in the P–F phase transition temperature with H, $\Delta\Theta_f = \Theta_f(H) - \Theta_f(0)$. *H:* magnetic field. *E:* electric field employed in the capacitance measurements. Full circles, full triangles: melt-grown single crystals, full squares: high quality ceramics. Solid curves: results of least squares fits using $\Delta\Theta_f = \alpha H^2 + \beta H^4$.

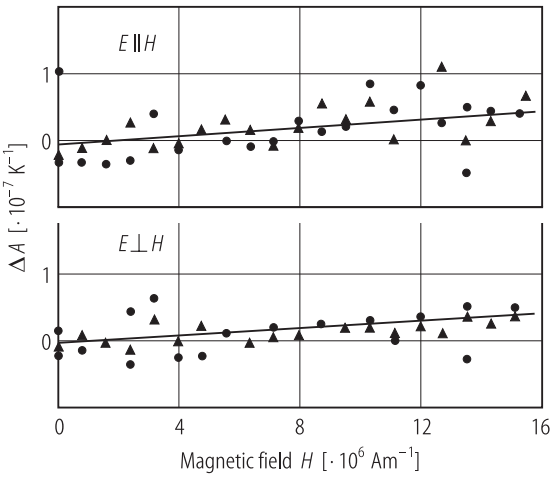

Fig. 1A-10-196. $BaTiO_3$. ΔA vs. H [81Wag]. ΔA*:* change in slope in the $1/\kappa$ vs. T curves with H, $\Delta A = (d/dT)[1/\kappa(H) - 1/\kappa(0)]$. *H:* magnetic field. *E:* electric field employed in the capacitance measurements. Full circles, full triangles show difference of used single crystals.

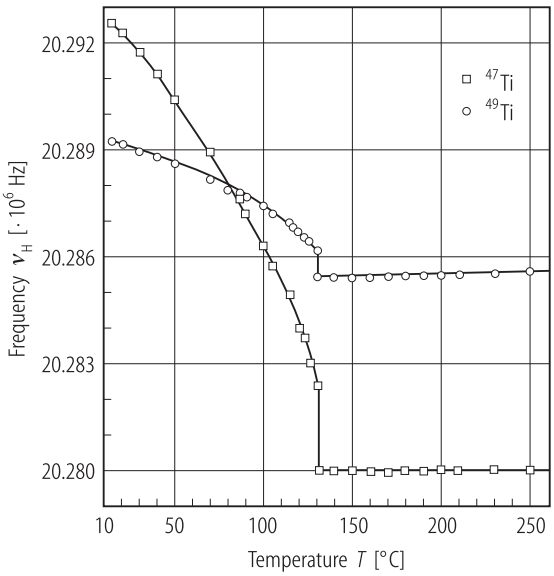

Fig. 1A-10-197. $BaTiO_3$. ν_H vs. T [94Kan]. ν_H: NMR frequency of ^{47}Ti and ^{49}Ti. Single domain crystal grown by the top-seeded solution method. Magnetic field is perpendicular to the *c*-axis.

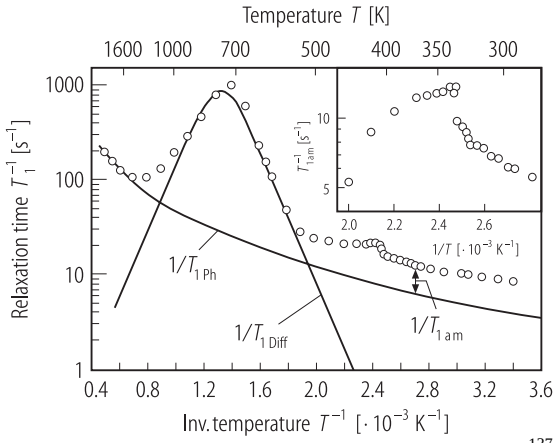

Fig. 1A-10-198. $BaTiO_3$. $1/T_1$ vs. $1/T$ [94Kan]. T_1: ^{137}Ba spin-lattice relaxation rate estimated from NMR spectra. The data plots are interpreted as the sum of three contributions: a phonon contribution ($1/T_{1Ph}$), a diffusion-induced contribution ($1/T_{1Diff}$) and a contribution related to dynamics of additional modes ($1/T_{1am.}$). Insert shows $1/T_{1\cdot a.m.}$ in the vicinity of Θ_f.

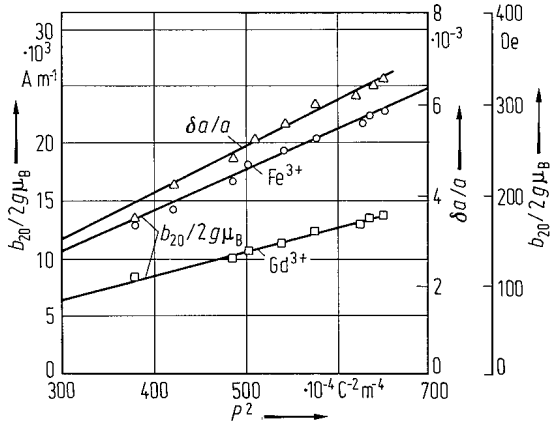

Fig. 1A-10-199. $BaTiO_3$: Gd^{3+}. $b_{20}/2g\mu_B$, $\delta a/a$ vs. P^2 [62Rim]. $b_{20}/2g\mu_B$: spin Hamiltonian parameter. $\delta a/a$: piezoelectric strain (δa is the change in transverse direction perpendicular to P, a is edge of the initial cubic unit cell). For comparison, $b_{20}/2g\mu_B$ of Fe^{3+} is also shown.

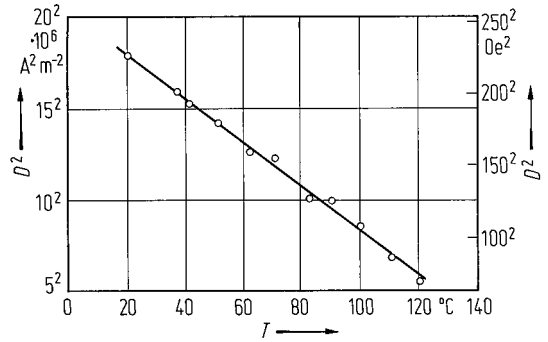

Fig. 1A-10-200. $BaTiO_3 : Mn^{2+}$. D^2 vs. T [65Ves]. *D:* spin Hamiltonian parameter of Mn^{2+}.

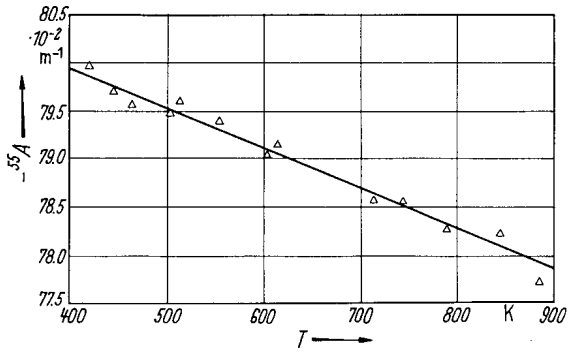

Fig. 1A-10-201. $BaTiO_3$: Mn^{2+}. $-^{55}A$ vs. T [67Zda2]. *A:* hyperfine coupling constant of Mn^{2+} in the cubic phase. Solid curve:

$$A(T) = A^0 - A^0 C T^4 \int_0^{\Theta_D/T} x^3 / \left(e^x - 1\right) dx$$

$A^0 = A(T = 0) = 81 \cdot 10^{-2}$ m^{-1}; $C = 1.71 \cdot 10^{-12}$ K^4; Debye-temperature $\Theta_D = 450$ K.

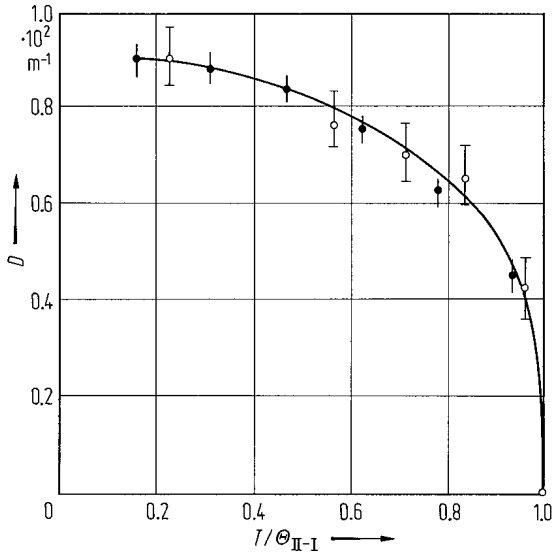

Fig. 1A-10-202. $BaTiO_3$: Fe^{3+}. D vs. T/Θ_{II-I} [72Mag].
D: spin Hamiltonian parameter of Fe^{3+}.

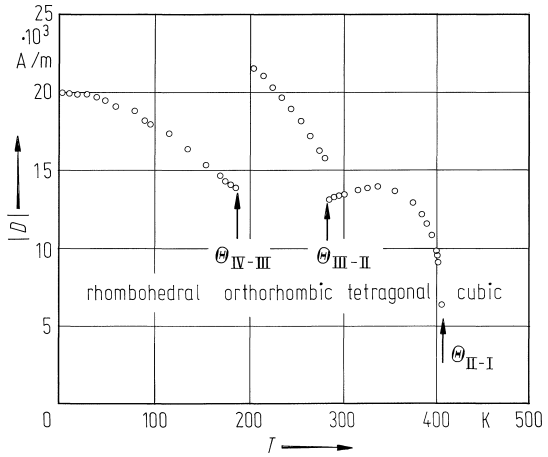

Fig. 1A-10-203. $BaTiO_3 : Cr^{3+}$. $|D|$ vs. T [85Mul]. *D:* spin Hamiltonian parameter of Cr^{3+}.

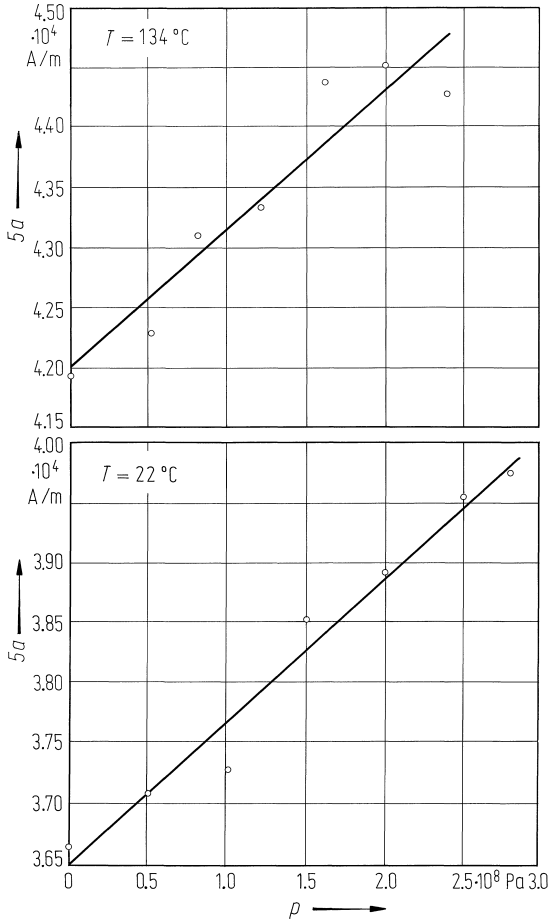

Fig. 1A-10-204. $BaTiO_3$: Fe^{3+}. 5*a* vs. *p* [86Mul]. 5*a:* cubic fine structure splitting of Fe^{3+}. Parameter: *T*.

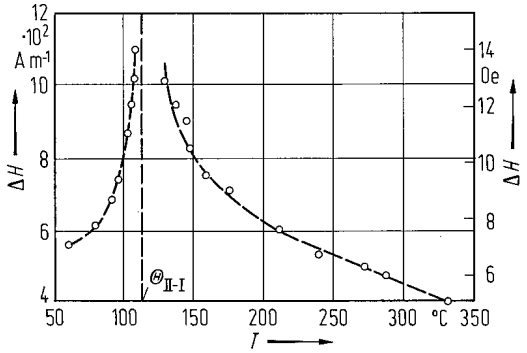

Fig. 1A-10–205. $BaTiO_3 : Mn^{2+}$. ΔH vs. T [73Sha]. ΔH: ESR linewidth of Mn^{2+} ($m = -5/2$, $M = -1/2 \rightarrow 1/2$).

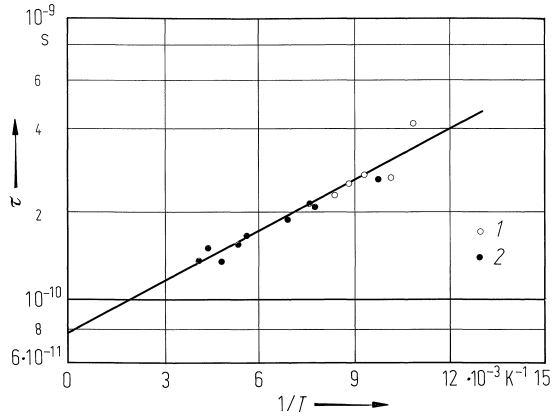

Fig. 1A-10-206. $BaTiO_3$: Pt^{3+}. τ vs. $1/T$ [81Buk]. τ: correlation time of Pt^{3+} ions. Open circles: calculated from the line-width at $H \parallel [100]$. Full circles: at $H \parallel [110]$.

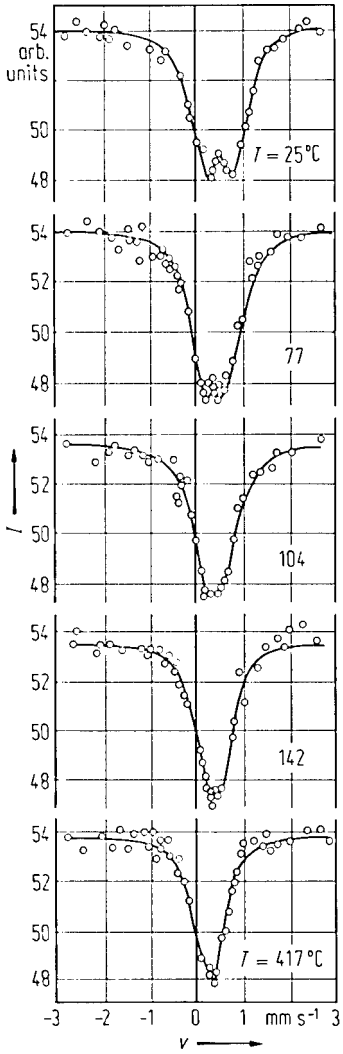

Fig. 1A-10-207. $BaTiO_3$: ^{57}Co. Mössbauer spectra [65Bhi]. Parameter: *T. I:* counting rate, *υ:* absorber velocity.

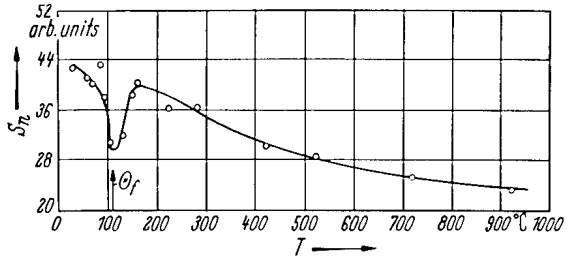

Fig. 1A-10-208. $BaTiO_3$: ^{57m}Fe. S_n vs. T [65Bhi]. S_n: normalized area of ^{57m}Fe source Mössbauer spectrum. ^{57m}Fe: second excited state of Fe nucleus.

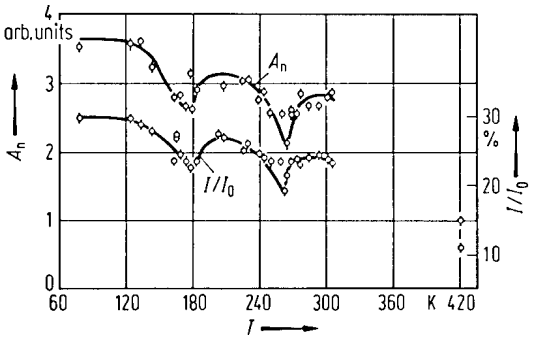

Fig. 1A-10-209. $BaTiO_3$: ^{119}Sn. Mössbauer effect. A_n and I/I_0 vs. T [72Bhi]. A_n: normalized area under resonance, I/I_0: absorption.

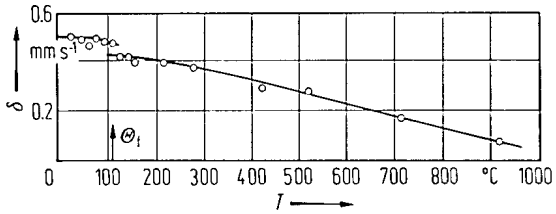

Fig. 1A-10-210. $BaTiO_3$: ^{57m}Fe. δ vs. T [65Bhi]. δ: isomer shift, relative to 310 stainless steel.

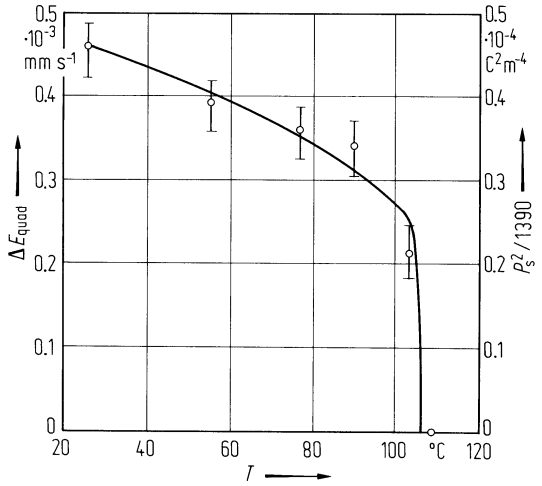

Fig. 1A-10-211. $BaTiO_3$: ^{57m}Fe. ΔE_{quad} vs. T [65Bhi]. The solid line indicates the variation of P_S^2 on a matching scale. ΔE_{quad}: quadrupole splitting. See also [85Her].

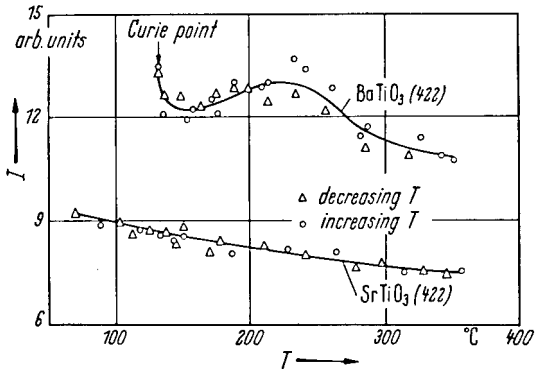

Fig. 1A-10-212. $BaTiO_3$ (powder). I(422) vs. T, in comparison with I(422) of $SrTiO_3$ [64Mot]. I(hkl): integrated Bragg intensity.

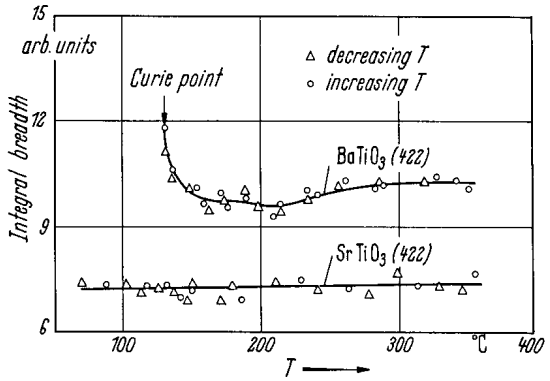

Fig. 1A-10-213. $BaTiO_3$ (powder). Integral breadth of (422) Bragg reflection vs. *T*, in comparison with that of (422) Bragg reflection in $SrTiO_3$ [64Mot].

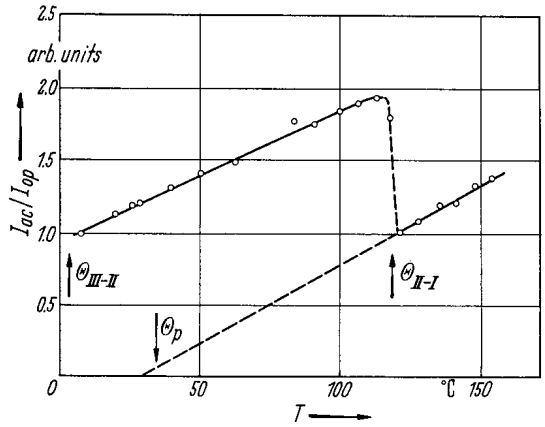

Fig. 1A-10-214. $BaTiO_3$. I_{ac}/I_{op} vs. T [67Har2]. I_{ac}: intensity of diffuse scattering due to acoustic phonons, I_{op}: that due to a transverse optic phonon. $I_{ac}/I_{op} \propto \nu_{op}^2$.

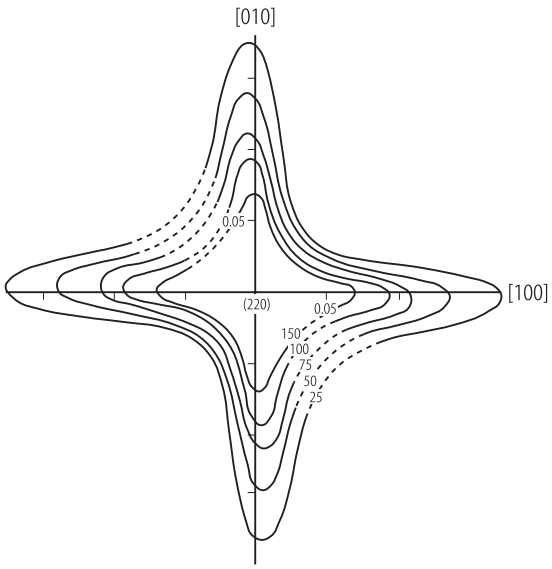

Fig. 1A-10-215. $BaTiO_3$. Intensity distribution of the quasi-elastic scattering in *q*-space around (220) [69Yam]. T = 137 °C.

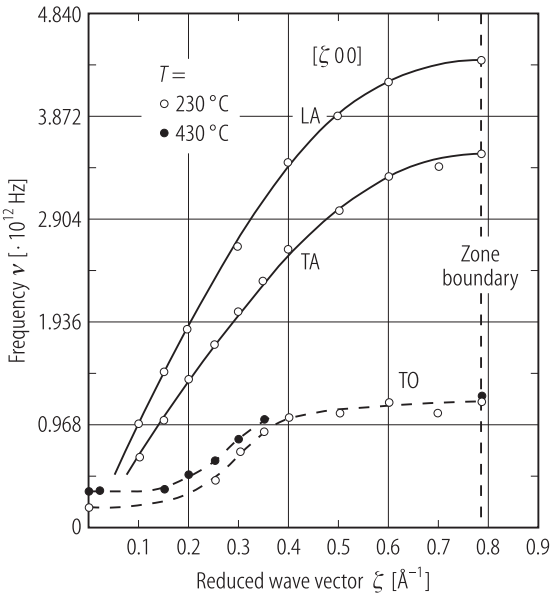

Fig. 1A-10-216. $BaTiO_3$. Phonon dispersion relation along [100] direction in the cubic phase [67Shi]. *v*: phonon frequency.

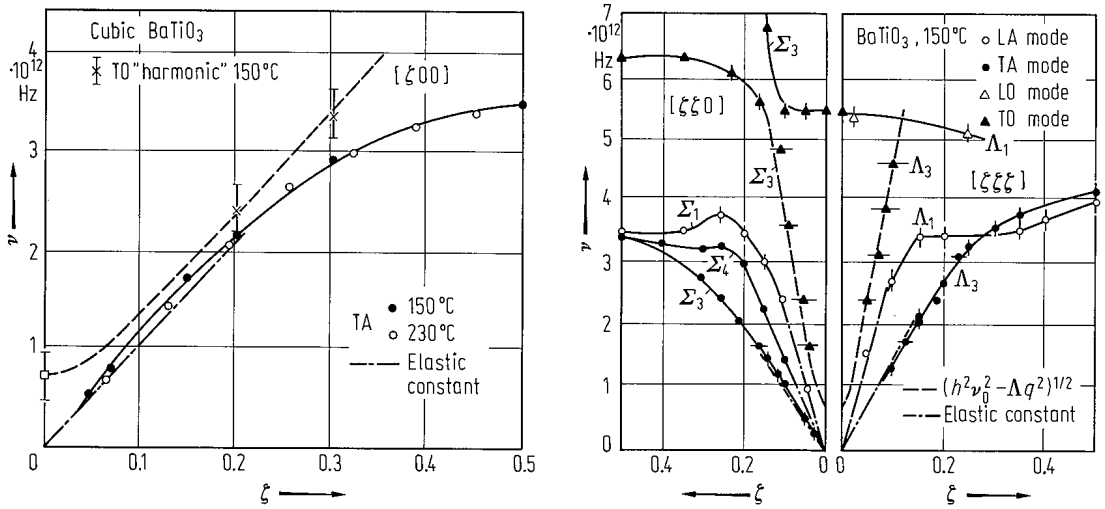

Fig. 1A-10-217. $BaTiO_3$. ν vs. ζ along [100], [110] and [111] directions at 150 °C [71Har]. ν: phonon frequency, ζ: reduced wave vector coordinate. For the optical branch with [ζ00] the quasi harmonic frequencies deduced from optical (square) or neutron-scattering (crosses) experiment are given. The dashed line is of the form $(h\nu)^2 = (h\nu_0)^2 + \Lambda q^2$.

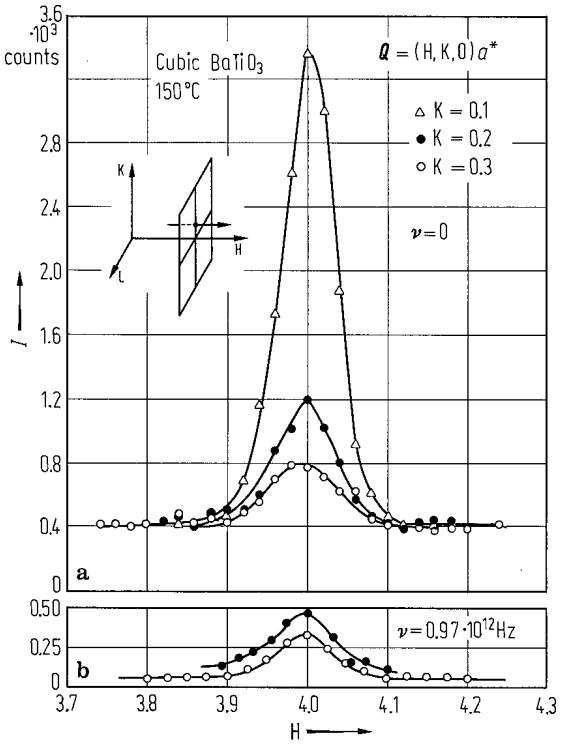

Fig. 1A-10-218. $BaTiO_3$. Triple-axis neutron spectrometer scans at constant frequency across the sheets of diffuse scattering at 150 °C [71Har]. The path of the scans is shown in the insert. The high background level in the elastic scan ($\nu = 0$) is due to nuclear incoherent scattering.

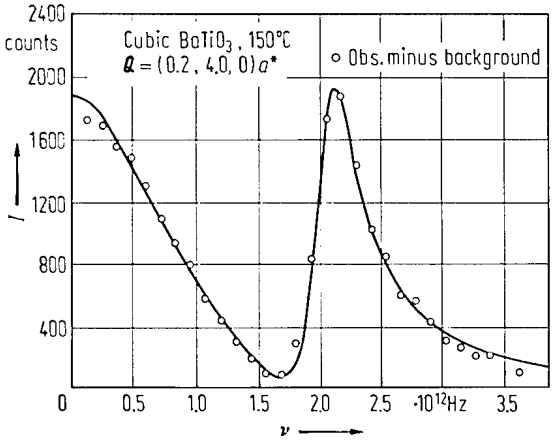

Fig. 1A-10-219. $BaTiO_3$. Typical profiles of the inelastic neutron scattering from the TA and the over-damped soft TO modes at 150 °C [71Har]. Incoherent elastic background is removed. The broad component centered about $\nu = 0$ is due to the over-damped soft TO mode. Solid line: calculated results.

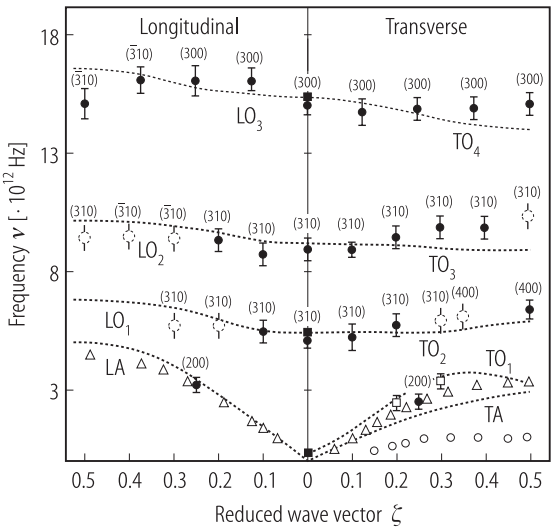

Fig. 1A-10-220. $BaTiO_3$. Phonon dispersion curves in the [00ζ] direction [79Bou]. *v:* phonon frequency. T =148 °C. For the symbol marks, see the original paper.

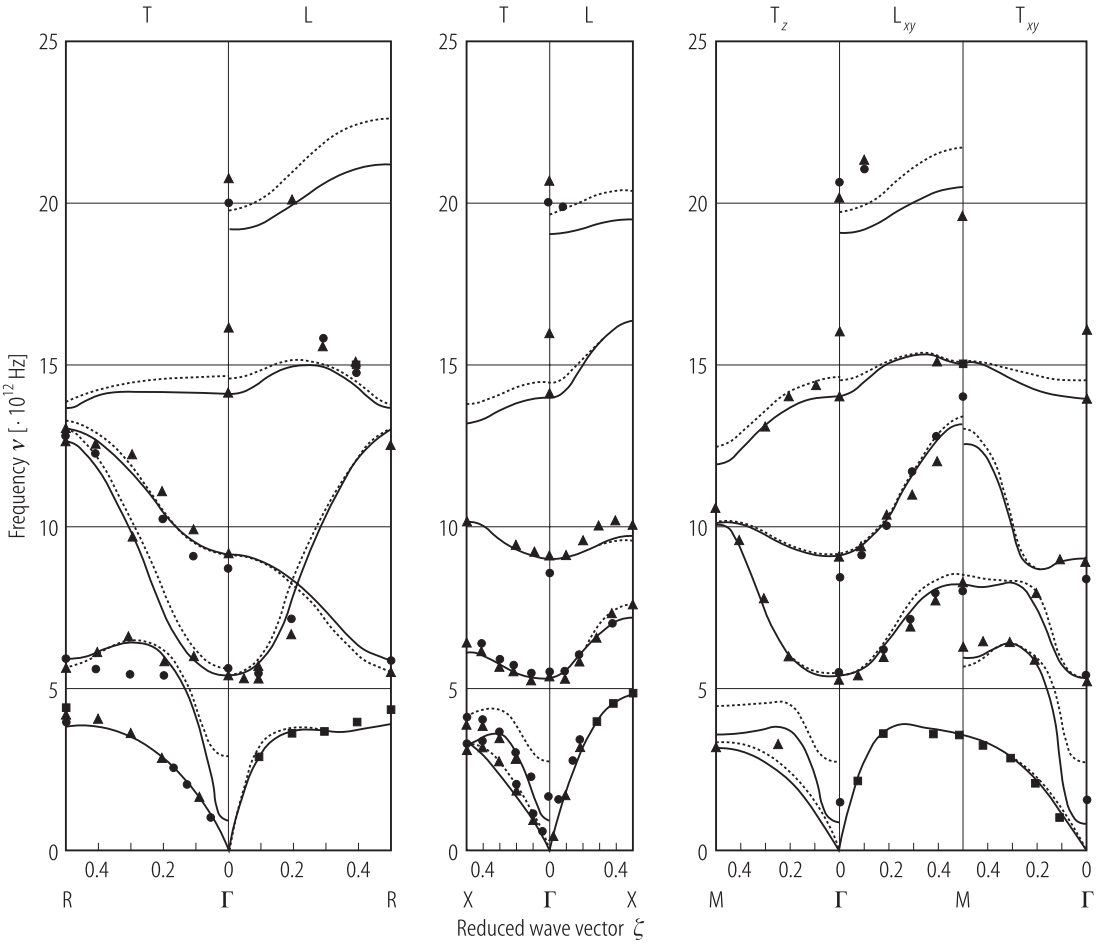

Fig. 1A-10-221. $BaTiO_3$, $Ba_{0.8}Sr_{0.2}TiO_3$. Phonon dispersion curves in the main symmetry directions [84Jan]. T = 473 K. *ν:* phonon frequency. Full triangle: undoped $BaTiO_3$, full circle: $Ba_{0.8}Sr_{0.2}TiO_3$, full square: undoped $BaTiO_3$ taken from [71Har]. Full curves: calculated curves in undoped $BaTiO_3$, broken curves: calculated ones in $Ba_{0.8}Sr_{0.2}TiO_3$.

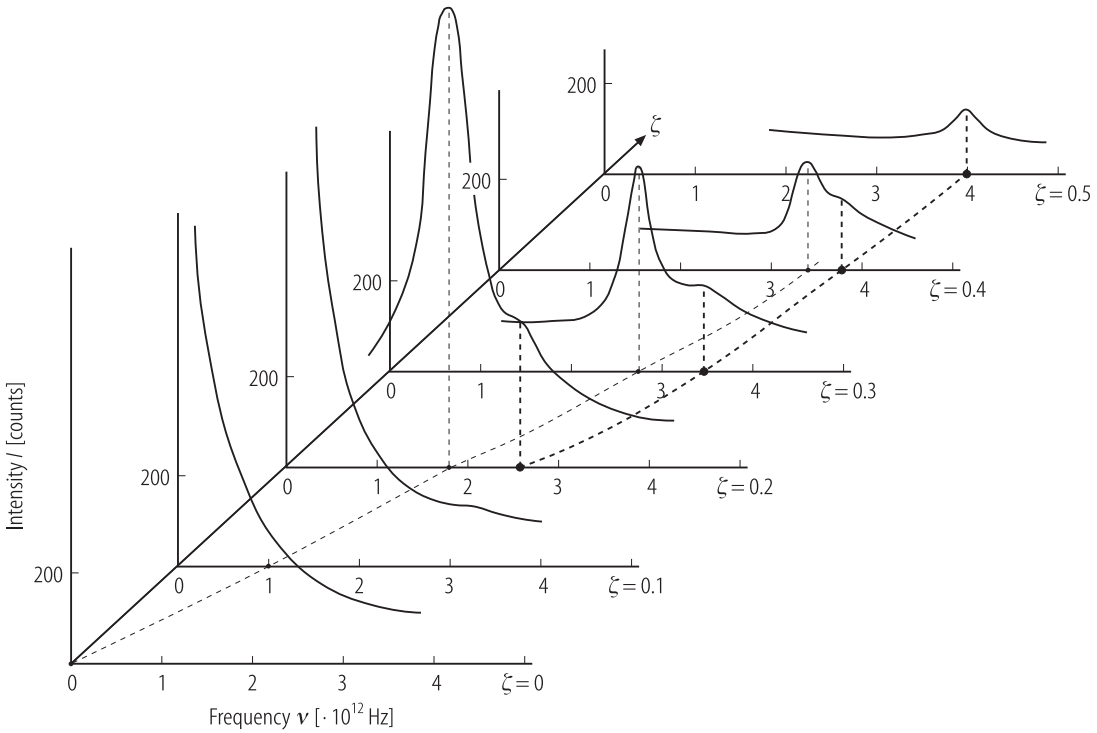

Fig. 1A-10-222. $BaTiO_3$. Low frequency transverse mode in the [00ζ] direction [84Jan]. T = 773 K. I: intensity of inelastic neutron scattering. ν: phonon frequency.

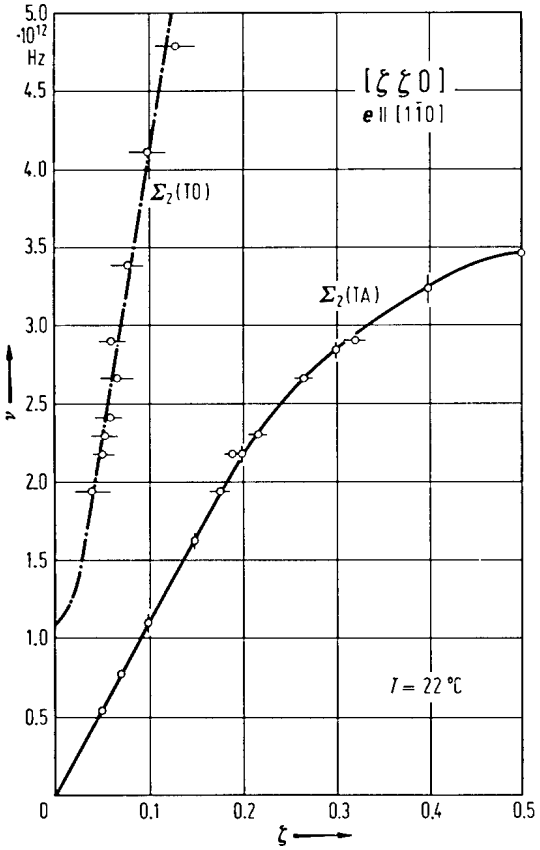

Fig. 1A-10-223. $BaTiO_3$. ν vs. ζ at RT [70Shi]. ν: phonon frequency. ζ: reduced wave number vector coordinate. e: polarization vector. The single domain crystal was produced by the top-seeded solution method.

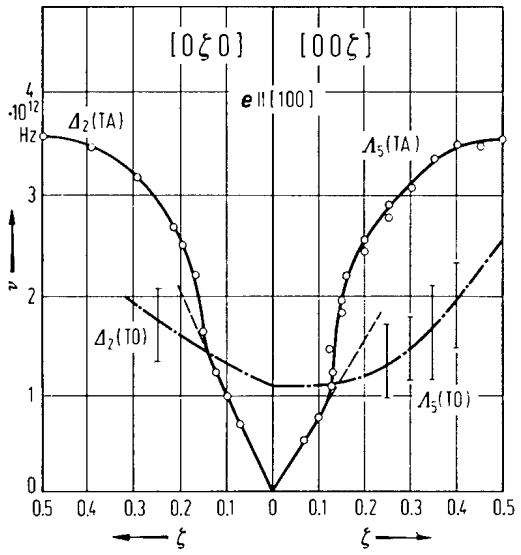

Fig. 1A-10-224. $BaTiO_3$. ν vs. ζ at RT [70Shi]. Symbols are the same as in Fig. 1A-10-223.

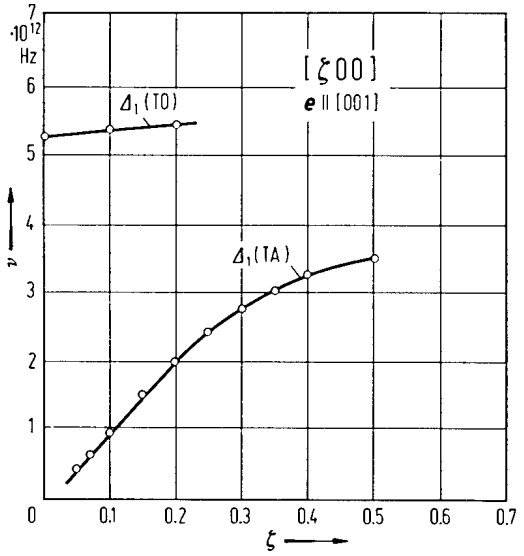

Fig. 1A-10-225. $BaTiO_3$. ν vs. ζ at RT [70Shi]. Symbols are the same as in Fig. 1A-10-223.

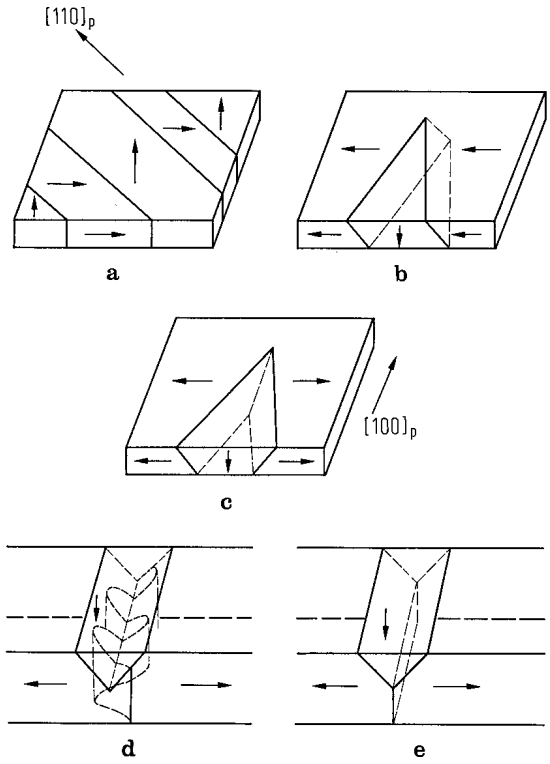

Fig. 1A-10-226. $BaTiO_3$. Several kinds of domain configurations observed in a {001} plate of tetragonal $BaTiO_3$ [64Tan]. Arrows represent the direction of the polar axis. **(a)** *a*–*a* 90° domains, **(b)**, **(c)** *a*–*c* 90° domains. **(d)**, **(e)** Wavy 180° domains. $[100]_p$, $[110]_p$ indicate the directions in pseudocubic cell.

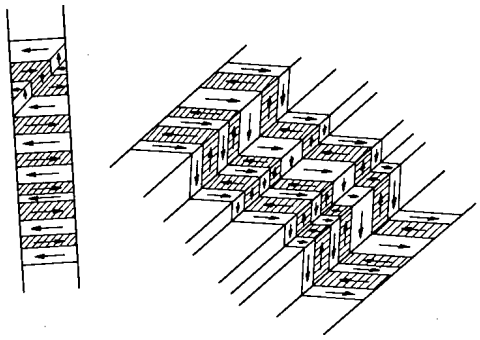

Fig. 1A-10-227. $BaTiO_3$. Complex domain structure of a strained $BaTiO_3$ plate in the tetragonal phase, showing 90^o and 180^o domain walls [55Hoo]. Arrows represent the direction of the polar axis.

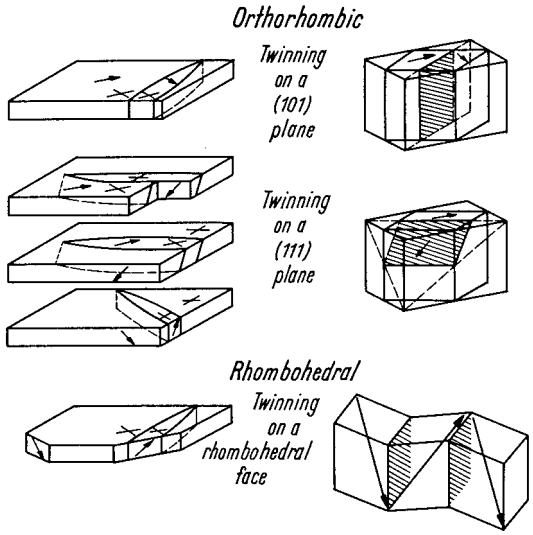

Fig. 1A-10-228. $BaTiO_3$. Geometry of the domains in the orthorhombic and rhombohedral phases [49For]. The arrows represent the direction of the polar axis. The plus signs and the crosses refer to parallel and symmetrical extinction, respectively.

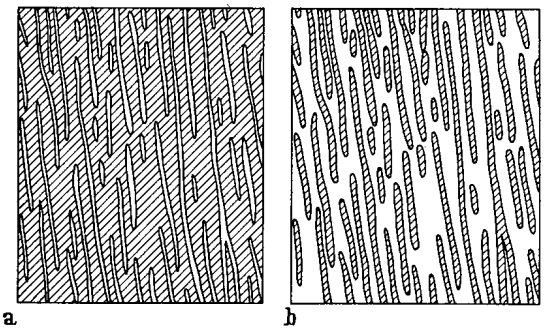

Fig. 1A-10-229. $BaTiO_3$. An example of complex domain structure of as grown crystals [55Can]. **(a)** Top surface, **(b)** bottom surface. These were revealed by HCl etching.

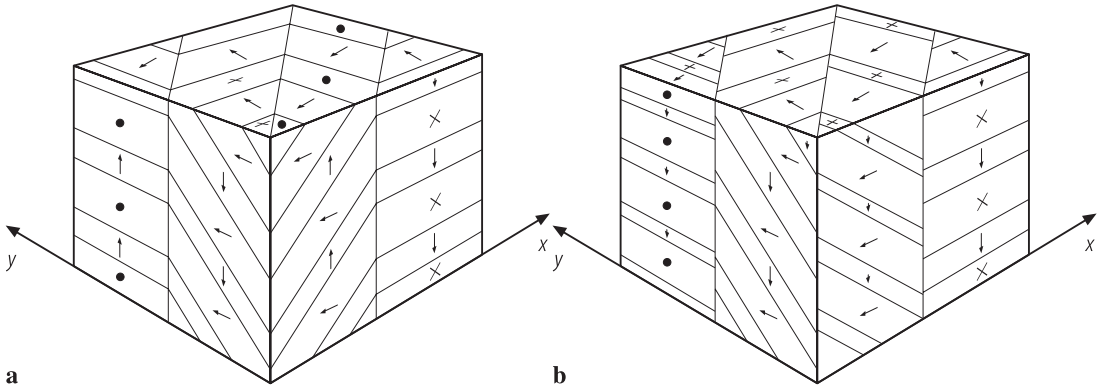

a **b**

Fig. 1A-10-230. $BaTiO_3$ (ceramics). Two types of domain configuration of cubic part of grain [80Arl]. Arrows indicate directions of polarization. (**a**) symmetrical. (**b**) asymmetrical.

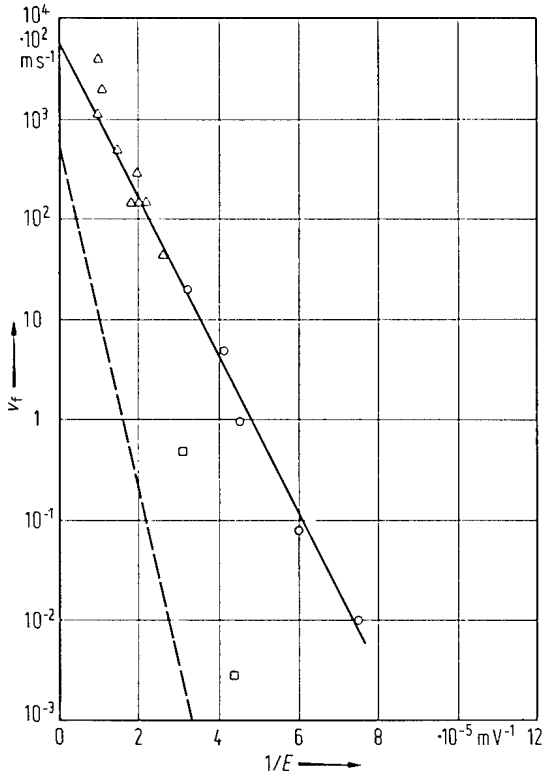

Fig. 1A-10-231. $BaTiO_3$. υ_f vs. 1/*E* [66Sta]. υ_f: forward velocity of 180° domain wall. The dashed line represents the sidewise velocity of 180° domain wall.

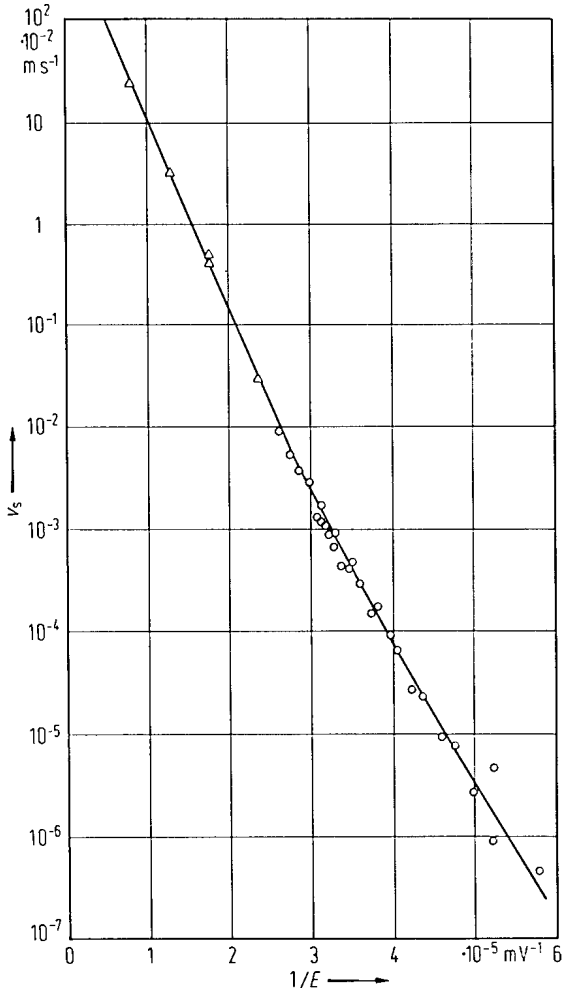

Fig. 1A-10-232. $BaTiO_3$. v_s vs. $1/E$ [59Mil]. v_s: sidewise velocity of 180° domain wall.

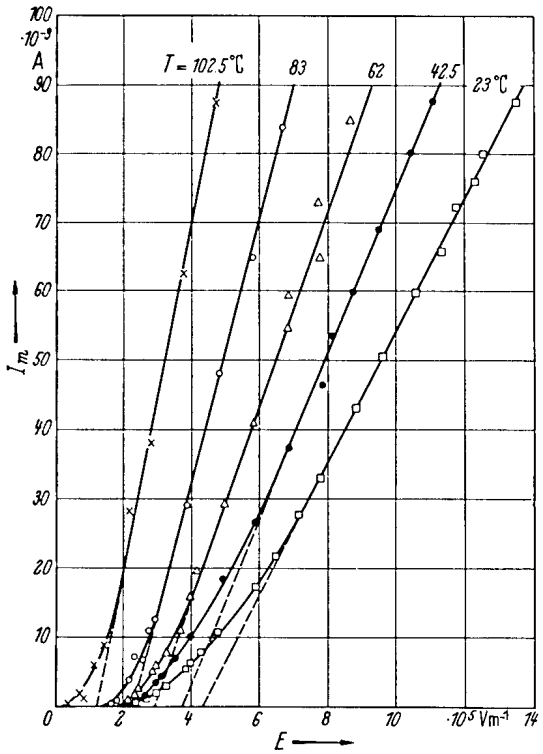

Fig. 1A-10-233. $BaTiO_3$. I_m vs. E [54Mer]. Parameter: T.
I_m: maximum switching current.

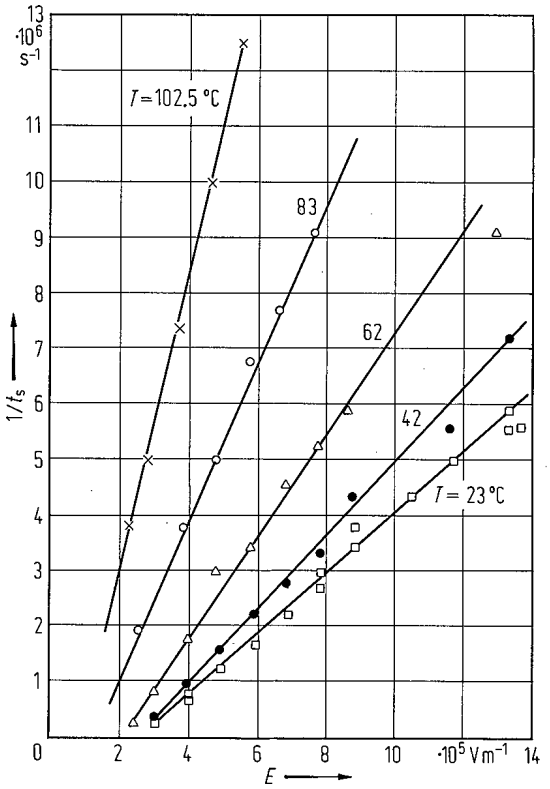

Fig. 1A-10-234. $BaTiO_3$. $1/t_s$ vs. E [54Mer]. Parameter: T.
t_s: switching time.

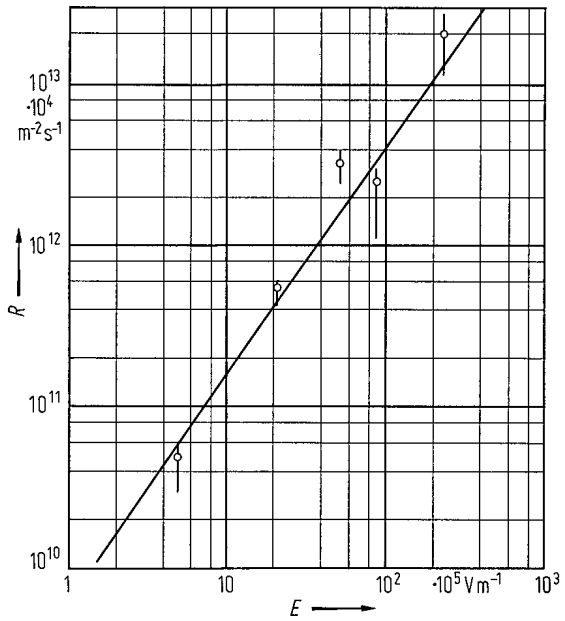

Fig. 1A-10-235. $BaTiO_3$. *R* vs. *E* [63Sta]. *R:* domain nucleation rate.

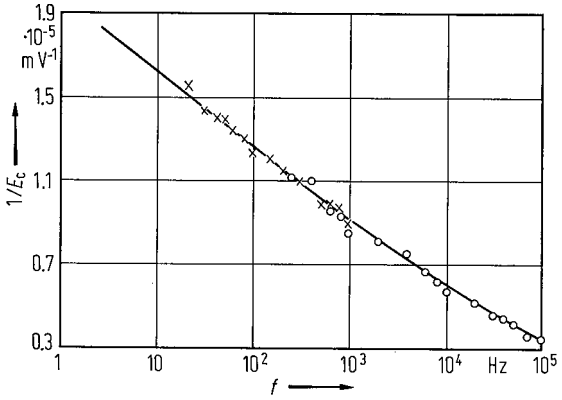

Fig. 1A-10-236. $BaTiO_3$. $1/E_c$ vs. f [58Pul].

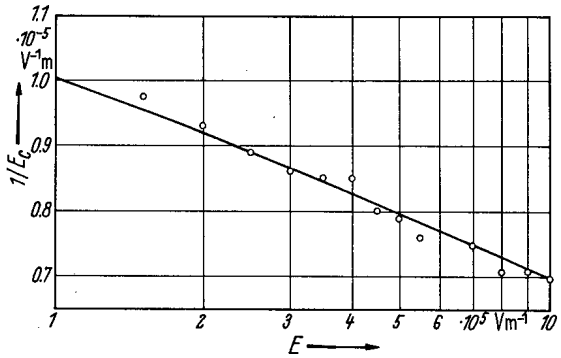

Fig. 1A-10-237. $BaTiO_3$. $1/E_c$ vs. E [58Pul]. f = 200 Hz, sinusoidal wave.

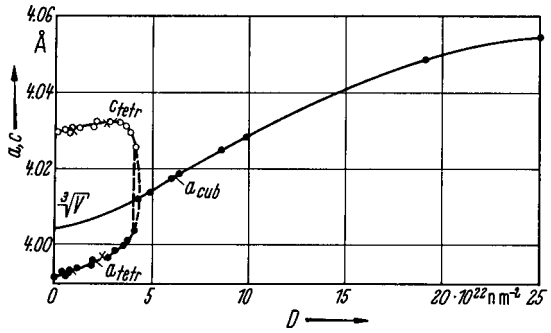

Fig. 1A-10-238. $BaTiO_3$. *a*, *c* vs. *D* [66Sch]. *D:* integrated neutron flux. n: number of neutrons.

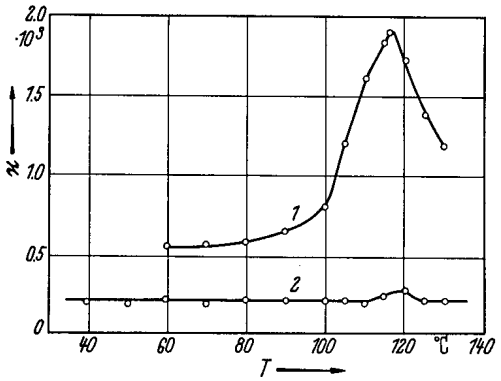

Fig. 1A-10-239. $BaTiO_3$ (ceramics). κ vs. T [56Rog]. Curve *1*: before irradiation, *2*: after pile irradiation $n\upsilon t = 2.1 \cdot 10^{20}$ (cgs). See also [62Hil]. $n\upsilon$: neutron flux [neutrons/cm^2 s]; t: irradiation time [s]. f = 1 kHz.